Journal of Magnetic Resonance 197 (2009) 1–8

Contents lists available at ScienceDirect

Journal of Magnetic Resonance

journal homepage: www.elsevier.com/locate/jmr

Flow imaging of fluids in porous media by magnetization prepared centric-scan SPRITE

Linqing Li [a,b], Quan Chen [a,1], Andrew E. Marble [a,2], Laura Romero-Zerón [c], Benedict Newling [a], Bruce J. Balcom [a,b,*]

[a] MRI Centre, Department of Physics, P.O. Box 4400, University of New Brunswick, Fredericton, NB, Canada E3B 5A3
[b] Department of Chemistry, P.O. Box 4400, University of New Brunswick, Fredericton, NB, Canada E3B 5A3
[c] Department of Chemical Engineering, P.O. Box 4400, University of New Brunswick, Fredericton, NB, Canada E3B 5A3

ARTICLE INFO

Article history:
Received 30 June 2008
Revised 23 October 2008
Available online 11 November 2008

Keywords:
MRI
SPRITE
Centric scan
Flow
Velocity
Single phase flow
Porous media
Sand pack
Pipe
Rock
Dispersion coefficient
q-Space

ABSTRACT

MRI has considerable potential as a non-destructive probe of porous media, permitting rapid quantification of local fluid content and the possibility of local flow visualization and quantification.

In this work we explore a general approach to flow velocity measurement in porous media by combining Cotts pulsed field gradient flow encoding with SPRITE MRI. This technique permits facile and accurate flow and dispersion coefficient mapping of fluids in porous media. This new approach has proven to be robust in characterizing fluid behavior.

This method is illustrated through measurements of flow in pipes, flow in sand packs and flow in porous reservoir rocks. Spatially resolved flow maps and local fluid velocity distribution were acquired.

1. Introduction

MRI is potentially the most powerful analytical tool for noninvasive multidimensional visualization of flow and transport in porous media [1]. Numerous attempts have been made to measure local velocity in porous media by combining phase encoding of the velocity with fast imaging methods such as FLASH, EPI and RARE [2–4]. These methods employ frequency encoding gradients for spatial resolution. These gradients are naturally sensitive to the spin motion, yielding signal loss and phase deviation [5,6]. The large internal gradients induced by the susceptibility mismatch of the fluid and matrix in realistic porous media will cause artifacts in both the spatial encoding and velocity encoding processes. In addition, the short transverse relaxation time (T_2^*, T_2) of the fluids in porous media hampers the use of frequency encoding methods due to gradient strength limitations and relaxation limited resolution [7].

Most attempts at velocity imaging in porous media have relied on idealized porous media with long relaxation times [8–11] because of these difficulties. The pure phase encode spatial encoding developed in this work avoids the difficulties associated with frequency encoding position. SPRITE imaging methodologies, pure phase encoding methods, are highly insensitive to spin motion and largely immune to the internal gradient effects of porous media, yet readily visualize fluids in porous media with very short relaxation times.

In recent work [12], we have developed magnetization prepared centric-scan SPRITE methodologies to spatially resolve the molecular diffusion coefficient in porous media, allowing us to differentiate water and oil in such samples. An alternate SPRITE MRI method with flow sensitization has allowed us to develop a wind-tunnel style MRI measurement of fully turbulent flow [13].

In this work, we present a method which combines Cotts PFG velocity encoding, as a magnetization preparation, with centric-scan SPRITE MRI [14] for local velocity measurement in porous media. The Cotts PGSTE protocol used in this work is a combination

* Corresponding author. Address: MRI Centre, Department of Physics, P.O. Box 4400, University of New Brunswick, Fredericton, NB, Canada E3B 5A3. Fax: +1 506 453 4581.
E-mail address: bjb@unb.ca (B.J. Balcom).
[1] Present address: British Petroleum, Sunbury-on-Thames, TW16 7LN, United Kingdom.
[2] Present address: Department of Systems and Computer Engineering, Carleton University, 1125 Colonel By Drive, Ottawa ON, Canada K1S 5B6.

1090-7807/$ - see front matter © 2008 Elsevier Inc. All rights reserved.
doi:10.1016/j.jmr.2008.10.020

of the '13-interval, condition I' sequence of Cotts et al. [15] and the longitudinal eddy-current delay (LED) sequence of Gibbs and Johnson Jr. [16]. Cotts with LED is a powerful approach, which mitigates the influence of background magnetic field gradients in porous media and the potential phase errors caused by transient eddy-current fields. The essential idea is to use a velocity encoding preparation which is robust for porous media in combination with a robust spatial encoding method which is itself insensitive to flow.

The four-step phase cycle employed in our velocity mapping measurement directly merges the real and imaginary signals which are otherwise separated by the *z*-storage pulse. This phase cycle means the final images are complex-phase images. Separate images of the real and imaginary phase shift due to flow are not acquired saving experimental time, simplifying data handling and avoiding potential quadrature artifacts in the flow spectrum.

Cotts velocity encoding with centric-scan SPRITE for spatial encoding, yields a robust flow visualization tool, which is proven through measurements of pipe flow, flow in sand packs and flow in reservoir core plugs. Both spatially resolved flow maps and local fluid velocity distributions can be acquired.

The combination of Cotts PFG with centric-scan SPRITE spatial encoding will permit flow velocity mapping in a wide variety of realistic porous media accessible to current MRI flow imaging methods. One promising area of application will be fluid flow in petroleum reservoir core samples.

2. Theory

2.1. Flow encoding for centric-scan SPRITE

The SPRITE MRI technique is specifically designed for short MR relaxation times and will work with T_2^* lifetimes (as well as T_1, T_2 lifetimes) which are well under 1 ms. The advantages of centric-scan SPRITE compared to previous implementations of SPRITE [17] are profound: simplified image contrast is achieved, faster, with a better signal to noise ratio and a reduced gradient duty cycle.

As illustrated in Fig. 1, Cotts pulsed field gradient (PFG) preparation will yield flow information that can be spatially resolved. The local image intensity can be represented by the following equation:

$$S = \rho_0 f(\text{flow}) \exp\left(-\frac{t_p}{T_2^*}\right) \sin\theta, \quad (1)$$

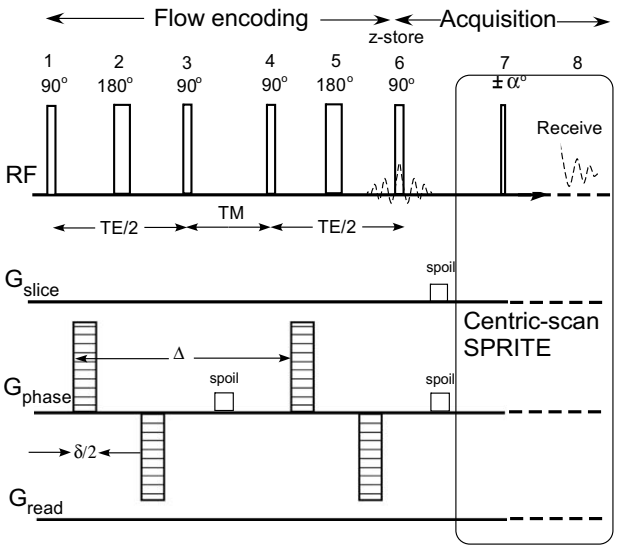

Fig. 1. Cotts PFG pulse sequence for flow encoding magnetization preparation with centric-scan SPRITE readout.

where f(flow) is the phase change and signal attenuation induced by the PFG preparation; ρ_0 is the spin density; t_p is encoding time; θ is the flip angle of the RF pulse.

Stimulated echoes are advantageous with $T_1 \gg T_2$ systems as, typically, encountered for fluids in porous media [18]. We employ pulsed field gradients and stimulated echoes as suggested by Cotts because background gradients associated with the medium, due to pore matrix susceptibility mismatch, will complicate a simple PFG velocity measurement. This method eliminates contributions from the cross-term ($g_0 g_a$) between the background gradient, g_0, and the applied gradient, g_a. Spoil gradients were used to eliminate residual transverse magnetization after the *z*-storage pulses. Potential phase errors caused by transient eddy-current fields are avoided by the implementation of the LED protocol in which the stimulated echo is stored longitudinally for a period long enough for the transient eddy-current fields to decay. The final *z*-storage pulse yields flow encoded signal for centric-scan SPRITE read out and spatial encoding.

2.2. Velocity mapping

Dynamic imaging will be performed by successively stepping the Cotts PFG gradients for n steps to some g_{max} value; n is necessarily small given the total imaging time.

Our measurements of fluid flow are time averaged in two senses. The technique records displacements during the observation time (Δ, Fig. 1) and reported velocities average fluid behaviors during that interval. Additionally, the velocity measurements require n measurements made over several minutes and any unsteadiness in the flow on that time scale is also averaged in reported velocities.

2.2.1. SPRITE velocity imaging phase cycle

In most previous studies, the flow shifted signal phase was *z*-stored and imaged separately as the sine component and the cosine component [23]. Individual pixels from real and imaginary MRI images are then combined into a new set of complex images during data processing. The q-space transformation is then performed successively for each pixel.

Instead of recombining individual real and imaginary images during the data processing stage, we recombine the real and imaginary signal in the phase cycle. This phase cycle avoids variation of the initial phase of the $q = 0$ point and removes potential imperfections which could cause a quadrature image of the main velocity peak [19]. The phase cycle is outlined in Fig. 1 and Table 1. The analogous phase cycle previously employed by others for bulk measurements [21–23], can only be used in acquisition of the real and imaginary images separately. However, by shifting the phase of one RF pulse (pulse #7 in Fig. 1) from x to y, this problem is solved. We further simplify the Table 1 phase cycle into a four step

Table 1
Full phase cycle for flow measurement in Cotts + SPRITE sequence

Pulse number	Flip angle (°)	Phase cycle (16 steps)	
1	90	00112233	00112233
2	180	12233001	12233001
3	90	00000000	00000000
4	90	22332233	22332233
5	180	33003300	33003300
6	90	22222222	33333333
7	(90 or α)[a]	00000000	11111111
8	Receiver	02022020	02022020

[a] 90° for FID bulk measurement, α for Cotts + SPRITE imaging acquisition sequence.

phase cycle, Table 2, which yields results with no appreciable artifacts.

The flow chart in Fig. 2 shows the process of MR velocity imaging and explains the phase cycle. The 90° z-storage pulse along x- and $-y$- direction introduces a phase factor, "1" for the cosine component and "i" for the sine component. The final signal in each image pixel will be $M = M_{(P)}\exp[-i(\theta+\psi)]$ where θ is the phase shift due to flow and ψ is the phase due to imaging gradient.

2.2.2. Velocity map from unwrapped phase

In cases where the image acquisition speed is critical, and the velocity in each pixel is unique, one could calculate the velocity from the slope of the phase change with the gradient amplitude in each individual pixel. The relationship between phase and velocity is shown in the following equation:

$$\Phi = \gamma g v \delta \Delta, \tag{2}$$

where ϕ is the phase induced by the velocity; γ is gyromagnetic ratio; g is the velocity encoding gradient; v is the flow velocity in direction of g; δ is the PFG gradient encoding time; Δ is the spin evolution time.

The rate of change of phase with flow encoding gradient g, $d\phi/dg$, can be used as a simple method for determination of velocity through Eq. (2). The sign of the slope indicates the flow direction. By this method, the number of gradient steps n can be limited. In the case of turbulent flow or highly dispersed flow, each individual pixel contains a distribution of phase which depends on the variety of flow histories of spin ensembles contained within the pixel. Fourier transformation along the flow gradient direction allows one to obtain a velocity spectrum at each pixel.

3. Results and discussion

3.1. Pipe flow measurements

Simple 2D imaging of pipe flow was undertaken to evaluate the potential for velocity mapping by using the pulse sequence of Fig. 1 and the phase cycle of Table 2. The images acquired were 2D spatial images with velocity encoding in the *z-direction* of the flow (along the horizontal bore of the magnet, parallel to the pipe axis). The flow velocity map from two straight tubes, with opposite flow direction, is displayed in Fig. 3a. The distorted ends of the two tubes in the velocity map are due to the gradient nonlinearity at the edge of the field of view. This distortion has no influence on the results. The mass balance for verification of the velocity map must follow the following equations:

$$v_m = \sum_i v_i \times \frac{I_i}{I_0}, \tag{3}$$

$$v_{act} = \frac{Q}{A\phi}. \tag{4}$$

Table 2
Short version phase cycle for flow measurement in Cotts + SPRITE sequence

Pulse number	Flip angle (°)	RE	Phase cycle (4 steps)	IM
1	90	0 1		0 1
2	180	1 3		1 3
3	90	0 0		0 0
4	90	2 3		2 3
5	180	3 0		3 0
6	90	2 2		3 3
7	(90 or α)[a]	0 0		1 1
8	Receiver	0 2		0 2

[a] 90° for FID bulk measurement, α for Cotts + SPRITE imaging acquisition sequence.

The velocity v_m is the average velocity through the pipe cross-section, Fig. 3a, marked by the solid line; i indexes the pixels along the solid line in one of pipes; v_i is the velocity of the chosen pixel; I_i/I_0 is the ratio of the individual pixel signal intensity to the total signal intensity of all the pixels along the line. Because SPRITE is insensitive to motion, the imaging pulse sequence, Fig. 1, with zero flow encoding gradient yields spin density images which are identical to the images acquired without flow. Therefore, I_i and I_0 should be determined from the flow image acquired with no flow encoding gradient; v_{act} is average velocity; Q is the actual volumetric flow rate which is set by the pump; A is the cross-sectional area of the tube; $\varnothing$ is the porosity. For pipe flow, $\varnothing$ is 1. The calculated result v_m from velocity mapping, Eq. (3), was 3.6 mm/s which agrees with the known velocity of 3.5 mm/s calculated from Eq. (4), within 3% error.

The flow variation across the tubes, extracted from the pixels marked by the solid line in Fig. 3a, is shown in Fig. 3b. We note the 2D image of Fig. 3a is that of a 3D object. The parabolic velocity maps of Fig. 3b are non-ideal in part due to this averaging. The flow in the tube was in the laminar flow regime. The signal intensity decay with g^2, shown in Fig. 3c, suggests a beating line due to the existence of multiple dispersion coefficients in that pixel. These data are extracted from the single pixel marked in Fig. 3a. The flow spectrum, Fig. 3d, reveals a skewed velocity distribution. A stagnant flow in the propagator is consistent with the spatial averaging of the flow.

It is easy to prove the reliability of the velocity distribution shown in Fig. 3d by comparing the intensity ratio of the maximum velocity and the stagnant flow in the spectrum Fig. 3d with the image intensity ratio of the center to two edges of the pipe in the *XY* view spin density image (not shown in the paper). From Fig. 3d, we observed that the intensity ratio between maximum velocity and stagnant flow was 2.6:1. Based on the intensity threshold chosen prior to the flow mapping, the intensity ratio between the center and two edges of the pipe in the *XY* view spin density images was 2.5:1. The two ratios agree very well. The flow spin density information extracted from *ZY* view flow images agrees with the spin density information in the *XY* view image.

Flow maps from the two pipes with an *XY* view are displayed in Fig. 4a. The pixel marked in Fig. 4a, shows a signal intensity decay, Fig. 4c, which is a straight line in the semi-log plot. The corresponding dispersion coefficient in the pixel is 4.5×10^{-9} m^2/s, larger than the self-diffusion coefficient of water. After FT of the complex data corresponding to the magnitude data of Fig. 4c, a sharp peak of the flow spectrum is shown in Fig. 4b. We do not observe a stagnant flow population in the *XY* flow propagator because the spatial averaging of these images is along the *z-direction*. The flow spectra from Figs. 3 and 4 are self-consistent and reliable.

Unwrapped phase information in Fig. 4d, extracted from marked pixels in Fig. 4a, could also be used to assign the velocity map according to Eq. (2). The sign of the slope of the unwrapped phase indicates the flow direction. The velocity calculated from these slopes are 5.5 and −4.5 mm/s, corresponding to the velocity calculated from the flow spectra of 5.8 and −4.5 mm/s, respectively.

It is possible to construct a simple velocity image by means of a single flow encoding step. Because of the motion insensitivity of SPRITE, when the imaging pulse sequence, Fig. 1, is employed with zero flow encoding gradient, both the spin density and the phase angle are identical between the images acquired with flow and without flow. Therefore, in systems where static conditions can be obtained, it is possible to use the phase of this unperturbed image to compute the velocity map from Eq. (2). In this case, only one gradient step will be used to determine the flow velocity mapping. One shot (plus a stationary image) velocity mapping of this type yielded similar images to those presented in Figs. 3 and 4a.

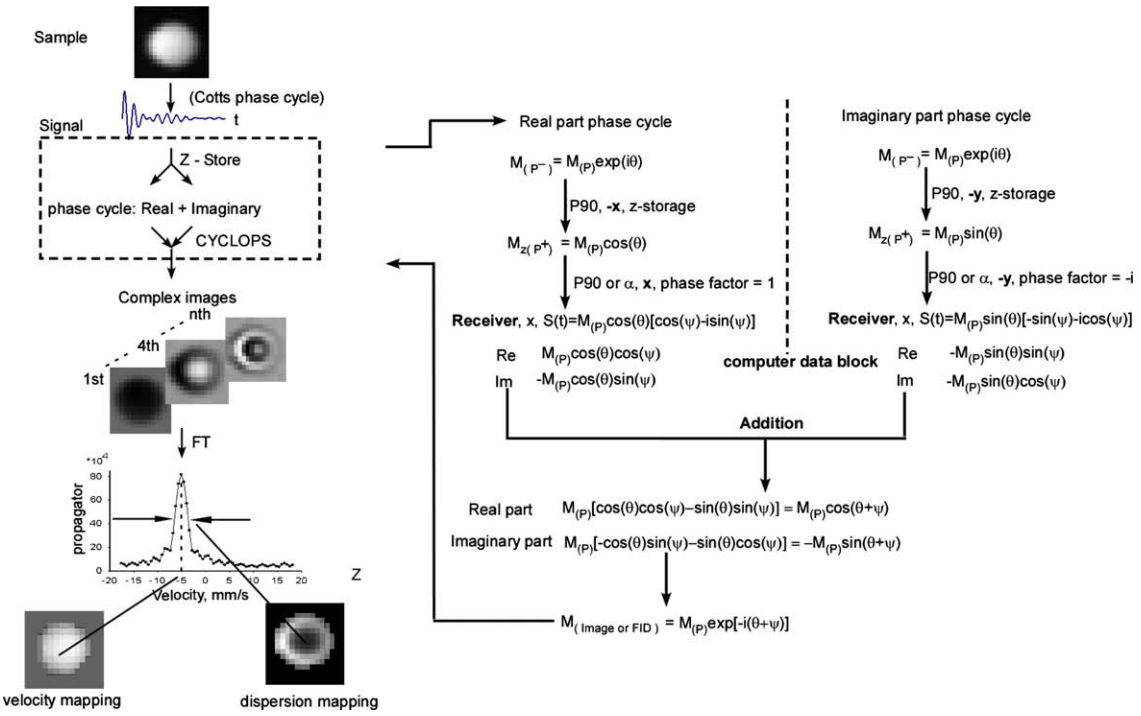

Fig. 2. Flow chart for MR velocity imaging and explanation of the phase cycle. The 90° z-storage pulse along x- and $-y$- direction introduces a phase factor, "1" for the cosine component and "i" for the sine component [20]. The final signal in each image pixel will be $M = M_{(P)}\exp[-i(\theta+\psi)]$ where θ is the phase shift due to flow.

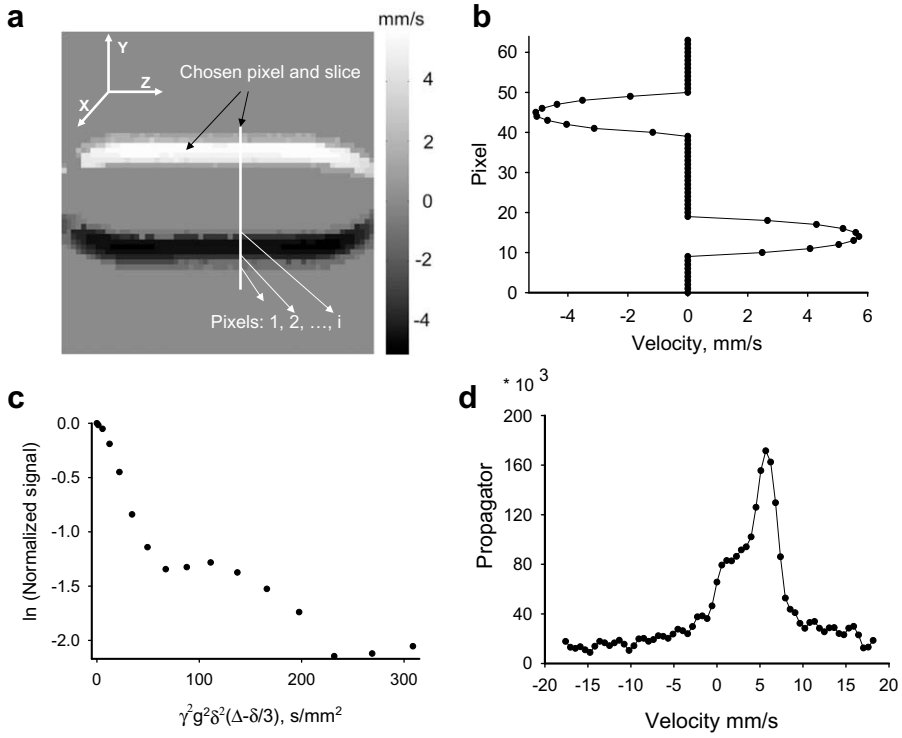

Fig. 3. (a) 2D pipe flow image with z-directed flow sensitization with a zy imaging plane. (b) 1D pipe flow map, extracted from the cross-sectional slice marked by a solid line in (a). The line in (b) joins the data points and as a guide to the eye. (c) Signal magnitude decay with g^2, extracted from the marked pixel in (a), indicates existence of flow dispersion in the pixel. (d) Flow propagator spectrum extracted from the marked pixel in (a). The skewed shape is due to the velocity distribution in the pixel.

3.2. Flow measurements in porous media

3.2.1. Flow measurements in sand pack

We undertook flow encoded 2D imaging of water in a sand pack, with a bulk flow rate of 10 ml/min, as a logical step from pure fluids to reservoir core studies. This flow rate corresponds to a Reynolds number of 0.14 with the sand pack employed. A 2D image of *z-directed* flow is displayed in Fig. 5a. The flow propagator extracted from the point marked in Fig. 5a is shown in Fig. 5b. Comparing Figs. 4 and 5b, the dispersion of flow in the sand pack is

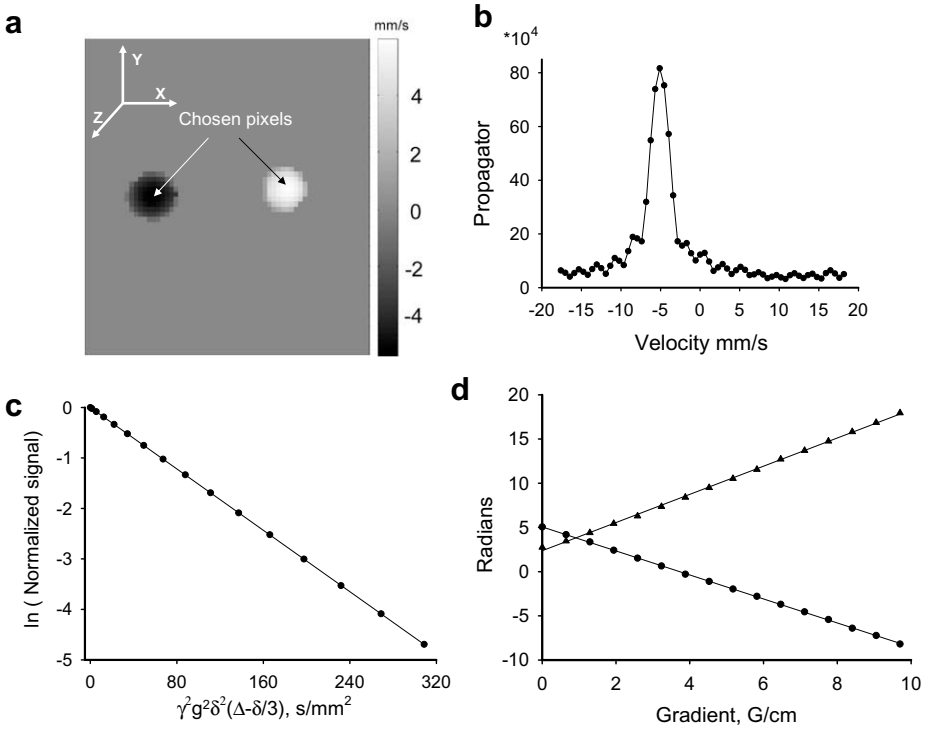

Fig. 4. (a) 2D pipe flow image with *z*-directed flow sensitization with the imaging plane *xy* of the identical system to Fig. 3. (b) Flow propagator spectrum extracted from the negative velocity pixel marked in (a) indicates a well defined velocity in the pixel. (c) Signal magnitude decay with g^2 extracted from the negative velocity pixel marked in (a), indicates a unique dispersion coefficient in the pixel. (d) Unwrapped phase extracted from the marked pixels in (a). The slope of the phase accumulation may be used for simple flow mapping as an alternative to taking the mode of the velocity spectrum.

greater than the dispersion in pipe flow, as expected for flow through a porous medium where the complex structure enhances dispersion of the fluids. The corresponding dispersion coefficient calculated from the half width of the spectrum in Fig. 5b is 9.2×10^{-9} m^2/s. Fig. 5c is a 1D profile extracted from the marked cross-sectional slice of the 2D velocity map in Fig. 5a. The average velocity, 0.86 mm/s, can be calculated from Fig. 5c according to Eq. (3). This result agrees with the known average velocity 0.81 mm/s calculated from Eq. (4) within 6% error.

In the 1D profile, high velocity pixels near the surface of the sample holder can be clearly observed. This is the result of a smaller resistance to flow between the smooth surface of the holder and the sand matrix. Unwrapped phase information in Fig. 5d, which is extracted from the marked pixel in Fig. 5a, could also be used to assign the velocity map according to Eq. (2). The velocity calculated from unwrapping the phase in Fig. 5d is 0.90 mm/s and the corresponding velocity calculated from the spectrum is 0.88 mm/s.

3.2.2. Flow measurements in reservoir core plugs

Our ultimate goal, flow velocity mapping in petroleum reservoir cores, was achieved by mapping water flow through a carbonate limestone. A photo of the core plug is reproduced as Fig. 6a. The constant injection flow rate was 2 ml/min. A 3D rendered view of the 3D flow map is provided in Fig. 6b. The 2D slice in Fig. 7a was extracted from one plane of the 3D *z*-directed flow map. The high velocity area in Fig. 7a, marked by a white square, suggests a high permeability channel.

Note that the flow map in Fig. 7a was displayed over a limited gray scale range to more clearly reveal the differences in flow within the rock. The limited number of velocity encoding gradient steps yields a limited number of velocity levels in the velocity spectrum. To prove we are observing a high permeability zone in the rock, we have sought complimentary evidence. A 2D slice from a 3D T_2 weighted static image is shown in Fig. 7b. We would hypothesize that a high permeability zone would correspond to a different rock matrix with a different T_2 distribution and that high permeability suggests a more open structure with longer average T_2. The high permeability region of Fig. 7a corresponds to the long T_2 region of Fig. 7b.

A 1D profile, Fig. 7c, was extracted from the region marked by the solid line in Fig. 7a to reveal the velocity variation more precisely. The maximum and the minimum velocity were 0.20 and 0.13 mm/s, respectively, a 35% difference. The average velocity calculated from Fig. 7c is 0.18 mm/s based on Eq. (3). The known velocity calculated from Eq. (4) is 0.2 mm/s.

The propagator, Fig. 7d, extracted from the marked pixel in Fig. 7a indicates the velocity in the pixel is 0.2 mm/s. The corresponding dispersion coefficient based on the half width of the spectra in the pixel is 9.0×10^{-9} m^2/s. Comparing this dispersion coefficient with the one acquired in flow in sand pack, we found both values are quite close to one another. However, note that the flow rate employed in the sand pack was 10 ml/min, 5 times larger than the flow rate of 2 ml/min employed in rock. The dispersion effect caused by matrix of the rock should be much larger than the effect caused by the matrix of the sand pack if the same flow rate was applied.

The flow rate 2 ml/min, we choose in this rock experiment, is much higher than the flow rate of 0.05 ml/min commonly employed in petroleum reservoir water flooding which translates to 2 feet/day. Laboratory MRI measurements are of necessity measurements of model samples and although reservoir flow rates are difficult to achieve, important flow phenomena may still be readily examined. The technique is readily capable of measuring much higher flow rates.

The fluid velocity measurement in rock suggests that the SPRITE velocity imaging measurement is very promising but will always

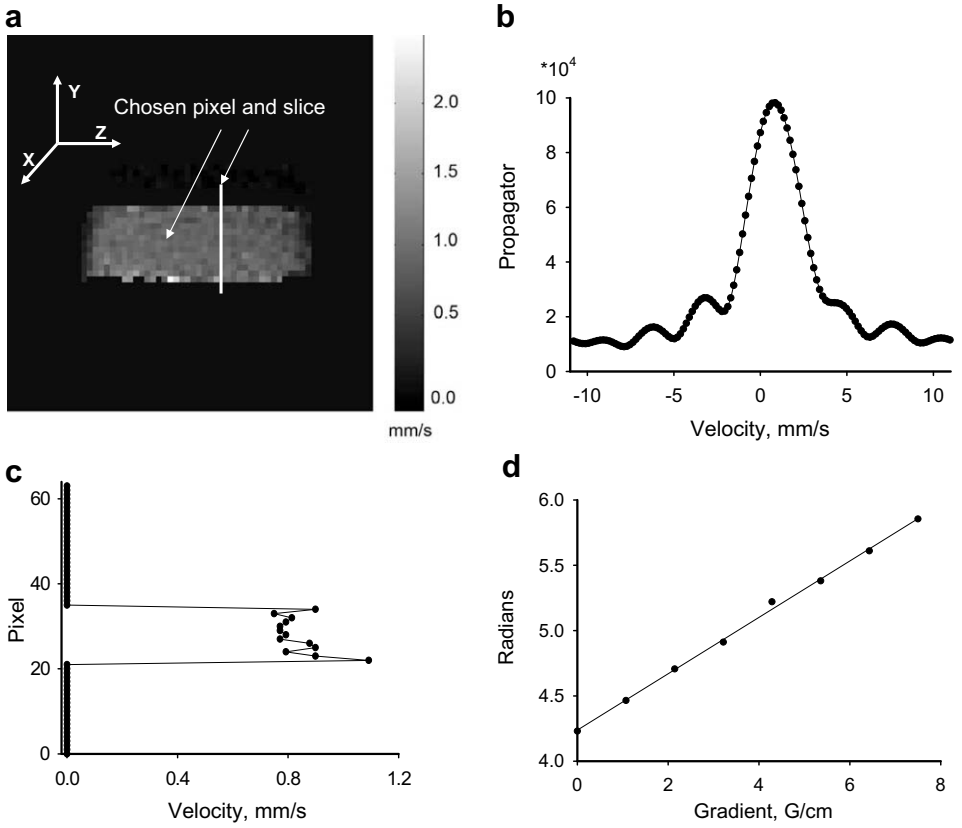

Fig. 5. (a) 2D single phase flow in sand pack with *z*-directed flow sensitization with the imaging plane *zy* and volumetric flow rate, 10 ml/min. (b) Flow propagator extracted from the marked pixel in (a). The propagator is much broader than observed in, Fig. 4, in which the pipe flow had higher flow rate. (c) 1D profile of the flow image extracted from the slice marked in (a). (d) Unwrapped phase extracted from the marked pixel in (a) indicates a high quality flow mapping.

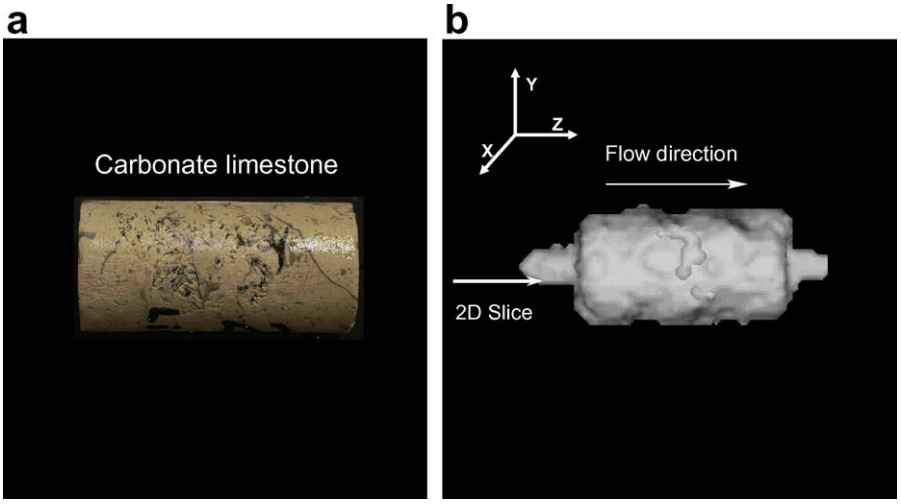

Fig. 6. (a) Photo of the carbonate limestone reservoir core plug. (b) 3D rendered image of the *z* velocity map of single phase flow in the carbonate limestone core plug.

be constrained by the relaxation time distribution. The relaxation times T_1 and T_2 are proportional to the pore size and the short T_2 component can be as short as a few milliseconds. In this case, some of the fluid signal will be lost in the flow encoding time, TE. This will cause not only reduced S/N but more importantly fail to encode the moving fluids which have very short T_2 value. On the other hand, the short T_2 fluid components in small pores or, clay bound and capillary water will be largely immobile in any case. Fluid components with T_2 values on the order of 5 ms and longer will be readily measured with these techniques.

Porous media experiments are ideally undertaken at low static field strength to increase the mean T_2. Since internal field gradients in porous media scale with the static field, it is advantageous to move to lower field and employ a simple PFG stimulated echo rather than the Cotts implementation to reduce the echo time. While lower static field will decrease the overall S/N, on balance we believe lower field is advantageous. At the same time high gradient strengths are advantageous so that the flow encoding time can be shortened as much as possible and lower flow rates can be measured.

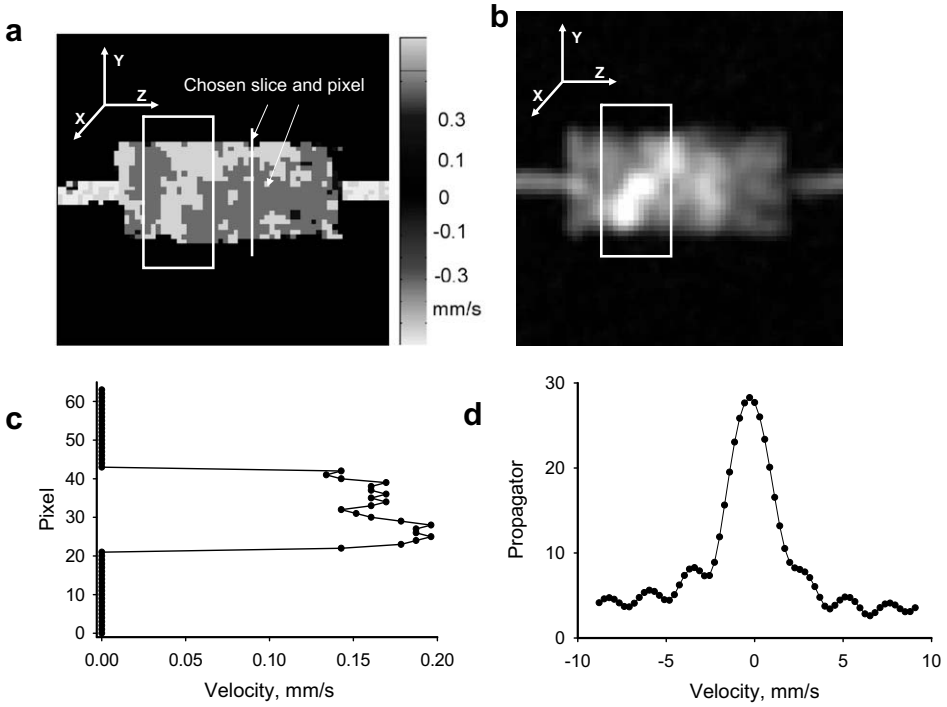

Fig. 7. (a) 2D slice from the 3D flow image. Flow is along the *z*-direction. A region of higher velocity, marked by the white square, indicated a high permeability channel in the rock. (b) 2D slice extracted from a 3D T_2-weighted image. The high intensity area, marked by the white square, indicates a high permeability channel as well. (c) 1D profile of the flow map extracted from the line in (a). (d) Propagator extracted from the marked pixel in (a).

4. Conclusion

Cotts PFG for flow encoding, combined with a centric scan pure phase encoding readout, based on the SPRITE methodology, is a powerful tool which can be applied to flow velocity imaging in porous media.

The biggest advantage of SPRITE compared to frequency encoding imaging is that SPRITE is highly insensitive to velocity. Paradoxically this is the most important factor to guarantee a high quality flow image. The velocity imaging is accomplished by flow encoding magnetization preparation.

Pipe flow was measured to evaluate the accuracy of this technique. Flow imaging in a 2D sand pack proved flow velocity imaging in porous media. Flow mapping in a 3D core reservoir shows the potential of this method for examining flow patterns and flow changes in realistic core samples, rather than idealized samples. Numerous flow imaging measurements of importance to reservoir core plug visualization, such as permeability mapping, tortuosity mapping, fracture flow visualization can be undertaken with these methods and visualization of the effects of permeability modification agents.

5. Experimental

All MRI measurements were performed on a DRX spectrometer (Resonance Instruments Ltd., Oxford, UK) with a 7 T, widebore, horizontal bore superconducting magnet 7 T/16/AS (Magnex Scientific Ltd., Oxford, UK). The standard micro-imaging gradient set SGRAD156/100/S (Magnex Scientific Ltd., Oxford, UK) employed was powered by a set of three Techron 7782 gradient amplifiers (AE Techron, Elkhart, USA), providing a maximum gradient strength of 38 G/cm. A home-made 62 mm inner diameter RF probe was used with the RF power amplifier 7T100S (Communication Power Corp., New York, USA). All measurement were undertaken at ambient temperature, 15 °C, in the magnet.

The Acciss and Jaims image processing packages, developed in the IDL programming environment by the UNB MRI Centre, were used for image reconstruction, image fitting and image display.

Sand (Shaw Brick, Fredericton, NB, Canada) employed in this study had grain size range of 200–800 μm, porosity 0.34, void ratio 0.68, specific gravity 2.39, and an estimated pore size of 200 μm.

The reservoir core plug sample was a carbonate limestone, surface coated by marine epoxy, with a porosity of 27.6%, 5.24 cm length, 2.5 cm diameter, low permeability rock 9 mD. After saturation with water, the relaxation times were $T_2^* = 500$ μs, $T_{2(1)}$ = 15 ms, 62%; $T_{2(2)}$ = 215 ms, 38%, and $T_{1(1)}$ = 30 ms, 78%; $T_{1(2)}$ = 615 ms, 21% with T_1 and T_2 fit to a bi-exponential relaxation model.

A high pressure pump QX-6000-SS (Vindum Engineering, San Ramon CA), was employed to provide constant flow through the pipe, sand pack and core samples in the experiments. These pumps permit direct selection of the volumetric flow rate which was confirmed by measurement of the outflow volume in select experiments.

Acquisition parameters for pipe flow and flow in sand pack were: sectoral SPRITE 2D-measurement 64 × 64, interleaves = 4, FOV = 80 × 80 mm, encoding time (t_p) = 100 μs, TR = 2 ms, flip angle = 4°. The delay between gradient interleaves was 1 s, acquisition time = 1 min, number of scans = 4, Δ = 20 ms, δ = 5 ms, the gradient g was along the direction of flow, z, with a maximum magnitude of 9.7 G/cm for pipe flow and 7 G/cm for flow in sand pack. The flow encoding gradient was incremented in 16 steps for pipe flow and 8 steps for flow in sand pack. The flow encoding data were zero filled to 64 points for pipe flow and to 128 for flow in the sand pack. The phase cycle was based on Table 2.

Acquisition parameters for flow in rock were: sectoral SPRITE 3D-measurement of: matrix 64 × 64 × 64, interleaves = 146, FOV = 80 × 80 × 80 mm, encoding time (t_p) = 200 μs, TR = 2 ms, flip angle = 4°. The delay between gradient interleaves was 500 ms, overall acquisition time = 5 h, number of scans = 8. The phase cycle was based on Table 2 with Δ = 12 ms, δ = 3 ms. The gradient g was paral-

lel to the direction of flow, z, with a maximum amplitude of 29.6 G/cm. The flow encode gradient was incremented in 8 steps with zero filling to 64 points.

For flow in sand pack experiments, a standard plastic 60 ml clinical syringe was cut to form the sample holder, 8.5 cm in length, 2.8 cm in diameter, packing porosity 34%. Water (distilled water) flow was 10 ml/min which corresponds to a Reynolds number of 0.14.

In the pipe flow experiments, two glass tubes were employed. Each was 1.1 cm in diameter and 100 cm in length. The entry length calculated from the ID and Reynolds number is 1.5 cm which is much shorter than the length of the tube. Doped water with $T_2 = T_1 = 100$ ms was employed to reduce the experimental time with a flow rate of 20 ml/min, Reynolds number 39.

The rock core sample was held under confining pressure with a Temco FCH Series MRI compatible core holder (Tulsa, Oklahoma). For flow in rock, the injection pressure and the confining pressure was provided by two high pressure pumps set at 60 and 150 psi, respectively. The flow rate was 2 ml/min.

Acknowledgments

The authors thank R.P. MacGregor, Murray Olive and Brian Titus for their technical assistance. Dr. Alexandre Khrapitchev, Dr. Igor Mastikhin, Dr. Ziheng Zhang, Mark Sankey, Dr. Murray Gingras and Drs. Yi-Qiao Song and Martin Hurlimann of Schlumberger-Doll are thanked for useful suggestions. B.J.B. thanks NSERC of Canada, the Atlantic Innovation Fund, Petroleum Research Atlantic Canada, CFI and the Canada Chairs program for funding. B.N. thanks NSERC of Canada and the Harrison McCain Foundation for support.

References

[1] P.T. Callaghan, Principles of Nuclear Magnetic Resonance Microscopy, Oxford University Press, New York, 1994.
[2] M. Rokitta, U. Zimmermann, A. Haase, Fast NMR flow measurements in plants using FLASH imaging, J. Magn. Reson. 137 (1999) 29–32.
[3] P. Mansfield, P.G. Morris, NMR imaging in biomedicine, Adv. Magn. Res. Suppl. 2 (1982) 1–343.
[4] J.J. Heras, A.J. Sederman, L.F. Gladden, Ultrafast velocity imaging of single and two phase flows in a ceramic monolith, Magn. Reson. Imag. 23 (2005) 387–389.
[5] E.M. Haacke, R.W. Brown, M.R. Thompson, R. Venkatesan, Magnetic Resonance Imaging Physical Principles and Sequence Design, Wiley, New York, 1999.
[6] E.M. Haacke, J.L. Patrick, Reducing motion artifacts in two-dimensional Fourier transform imaging, Magn. Reson. Imag. 4 (1986) 359–362.
[7] S. Gravina, D.G. Cory, Sensitivity and resolution of constant-time imaging, J. Magn. Res. B 104 (1994) 53–61.
[8] D. Guilfoyle, P. Mansfield, K. Packer, Fluid flow measurement in porous media by echo-planar imaging, J. Magn. Reson. 97 (1969) 342–358.
[9] R.A. Waggoner, E. Fukushima, Velocity distribution of slow fluid flows in Bentheimer sandstone: an NMRI and propagator study, Mag. Res. Imag. 14 (1996) 1085–1092.
[10] C. Chang, A. Watson, NMR imaging of flow velocity in porous media, AIChE 45 (1999) 437–440.
[11] L.D. Anadon, H.M. Lim, A.J. Sederman, L.F. Gladden, Hydrodynamics in two-phase flow within porous media, Magn. Reson. Imag. 23 (2005) 291–294.
[12] L. Li, F. Marica, Q. Chen, M.B. MacMillan, B.J. Balcom, Quantitative discrimination of water and hydrocarbons in porous media by magnetization prepared centric-scan SPRITE, J. Magn. Reson. 186 (2007) 282–292.
[13] B. Newling, P.C. Christopher, Z. Yang, R.A. James, C.J. Andrew, R. Dale, B.J. Balcom, Gas flow measurements by NMR, Prog. Nucl. Mag. Reson. Spectrosc. 52 (2008) 31–48.
[14] B.J. Balcom, R.P. MacGregor, S.D. Beyea, D.P. Green, R.L. Armstrong, T.W. Bremmer, Single-point ramped imaging with T_1 enhancement (SPRITE), J. Magn. Reson. A 123 (1996) 131–135.
[15] R.M. Cotts, M.J.R. Hoch, T. Sun, J.T. Marker, Pulsed field gradient stimulated echo methods for improved NMR diffusion measurements in heterogeneous systems, J. Magn. Reson. 83 (1989) 252–266.
[16] S.J. Gibbs, C.S. Johnson Jr., A PFG NMR experiment for accurate diffusion and flow studies in the presence of eddy current, J. Magn. Reson. 93 (1991) 395–402.
[17] M. Halse, D.J. Goodyear, M.B. MacMillan, P. Szomolanyi, D. Matheson, B.J. Balcom, Centric scan SPRITE magnetic resonance imaging, J. Magn. Reson. 165 (2003) 219–229.
[18] D. Le Bihan, Diffusion and Perfusion Magnetic Resonance Imaging, Raven Press, New York, 1995.
[19] P.B. Kingsley, Combining CYCLOPS with other phase cycles, J. Magn. Reson. A 110 (1994) 102–105.
[20] A.D. Bain, Coherence level and coherence pathways in NMR: a simple way to design phase cycling procedures, J. Magn. Reson. 56 (1984) 418–427.
[21] A. Jerschow, R. Kumar, Calculation of coherence pathway selection and cogwheel cycles, J. Magn. Reson. 160 (2003) 59–64.
[22] E.J. Fordham, S.J. Gibbs, L.D. Hall, Partially restricted diffusion in a permeable sandstone: observations by stimulated echo PFG NMR, Magn. Reson. Imag. 12 (1994) 279–284.
[23] M.H.G. Amin, S.J. Gibbs, R.J. Chorley, K.S. Richards, T.A. Carpenter, L.D. Hall, Study of flow and hydrodynamic dispersion in a porous medium using PFG magnetic resonance, Proc. R. Soc. Lond. A 453 (1997) 489–513.